In situ monitoring drying process to disclose the correlation between the molecular weights of a polymer acceptor with a flexible spacer and the

(article starts on next page)

Check for updates

In situ monitoring drying process to disclose the correlation between the molecular weights of a polymer acceptor with a flexible spacer and the performance of all-polymer solar cells†

Jiale Xiang,[ab] Sven Englund,[a] Zewdneh Genene, [ID][c] Guanzhao Wen,[d] Yanfeng Liu,*[ae] Nannan Yao, [ID][af] Rui Zhang, [ID][a] Leiqiang Qin, [ID][a] Lei Wang, [ID][a] Ergang Wang, [ID]*[c] Wei Zhang [ID]*[d] and Fengling Zhang [ID]*[ab]

Molecular weight (M_n) and conjugation of polymers can profoundly influence the performance of all-polymer solar cells (all-PSCs) *via* nanostructures of bulk heterojunctions (BHJs). To study the correlation between M_n and the performance of all-PSCs based on an acceptor with a flexible conjugation-break spacer (FCBS), three batches of acceptors, named PYTS, were synthesized with different number-average M_n from 9, 13 to 19 kDa. Blends with a polymer donor PBDB-T, the all-PSCs based on PYTS with M_n of 9 kDa and 19 kDa, exhibit power conversion efficiencies (PCEs) of 5.99% and 9.43%, respectively, primarily due to the increased short-circuit current density (J_{sc}) from 13.02 to 18.73 mA cm^{-2}. To disclose the impact of M_n on device performance, dynamics of mixed PBDB-T:PYTS solutions to solid BHJs is studied by monitoring the drying process with home-made *in situ* multifunctional spectroscopy, which demonstrates that PYTS with M_n of 19 kDa has a longer drying time than the PYTS with M_n of 9 kDa. Prolonged drying of the BHJs with higher M_n PYTS facilitates more tightly packed structures with higher crystallinity. A systematic investigation on the nanostructures of BHJs, charge generation, transport and recombination is carried out with grazing-incidence wide-angle X-ray scattering (GIWAXS), transient absorption spectroscopy (TAS) and characterization of all-PSCs. The results indicate that increased crystallinity in the BHJs benefits exciton dissociation, electron transport, prolonged carrier lifetimes, and decreased non-geminate recombination rate constants in the corresponding devices. Combining the *in situ* study of drying and the investigation on films and devices provides us a comprehensive understanding of the interplay between M_n, the drying process, the nanostructures of BHJs and device performance. This work not only emphasizes the essential role of M_n in governing the device performance, but also exhibits recorded film formation through the *in situ* spectroscopy, enabling us to manipulate the nanostructure of BHJs by optimizing M_n of polymers and processing parameters.

[a] Department of Physics, Chemistry and Biology, Linköping University, 58183 Linköping, Sweden. E-mail: fengling.zhang@liu.se

[b] Wallenberg Initiative Materials Science for Sustainability, Department of Physics, Chemistry and Biology, Linköping University, 58183 Linköping, Sweden

[c] Department of Chemistry and Chemical Engineering, Chalmers University of Technology, SE-41296 Göteborg, Sweden. E-mail: ergang@chalmers.se

[d] School of Physics and Materials Science, Guangzhou University, Guangzhou 510006, P. R. China. E-mail: wzhang@gzhu.edu.cn

[e] College of Materials and Textile Engineering, Nanotechnology Research Institute, Jiaxing University, Jiaxing 314001, P. R. China. E-mail: yanfeng.liu@zjxu.edu.cn

[f] State Key Laboratory of Silicon and Advanced Semiconductor Materials, Department of Polymer Science and Engineering, Zhejiang University, Hangzhou 310027, P. R. China

† Electronic supplementary information (ESI) available. See DOI: **https://doi.org/10.1039/d4tc02217c**

Introduction

All-polymer solar cells (all-PSCs), featuring the incorporation of polymeric donors (P$_D$s) and acceptors (P$_A$s) was first demonstrated in 1995 by A. J. Heeger's and A. B. Holmes' group, respectively.[1,2] An n-type polymer, with poly(pyridopyrazine vinylene) (EHH-PPyPzV) as the electron acceptor was synthesized by our collaborators M. R. Andersson and coworkers.[3] We fabricated all-PSCs using poly(2-methoxy-5-(20-ethylhexyloxy)-1,4-phenylenevinylene) (MEH-PPV) as the electron donor and EHH-PPyPzV as the electron acceptor, which presented an external quantum efficiency of 7% and an open circuit voltage of 900 mV under low-intensity monochromatic light.[4] Though some effort has been made, the development of all-PSCs has been hindered because the optical and electrical properties of

This journal is © The Royal Society of Chemistry 2024

J. Mater. Chem. C, 2024, **12**, 13029–13039 | **13029**

available acceptor polymers could not compete with dominating fullerene derivatives, such as $P_{71}CBMs$ and other non-fullerene acceptors (NFAs).[5–7]

With the emergence of NFAs, all-PSCs have regained considerable attention due to their intrinsic benefits, including their enhanced morphological stability, and improved mechanical properties over small molecular acceptor-based organic solar cells (OSCs).[8–13] Utilizing polymerized small-molecule acceptors (PSMAs), the power conversion efficiencies (PCEs) of all-PSCs have reached over 18%.[14–17] To increase the performance of PSCs, the development of an interlayer could also be important.[18–20] However, the unsatisfactory charge separation and transportation, which mainly originate from the undesirable bulk heterojunction (BHJ) morphology of active layers, lead to the low short-circuit current density (J_{sc}) and small fill factor (FF), hindering further advances in the photovoltaic performance of all-PSCs.[10,21–23] The morphology of BHJs is determined not only by the molecular aggregation of donors and acceptors, but also by their solubility in the processing solvent, aggregation rate and crystallization behaviors in solutions.[24,25] Given the solubility of conjugated polymers, the thermodynamics and crystallization kinetics[26–28] of all-polymer blends are profoundly affected by their number-average molecular weight (M_n) in contrast to small molecules,[29] elucidating the interplay between M_n, blend morphology and device performance is of crucial importance.

Most of the efforts made to reveal the effects of the M_n of P_DS and P_AS on the photovoltaic properties of all-PSCs mainly studied the morphologies of dried solid films and provided some interesting results.[30–35] It was found that increased M_n promoted the strong face-on packing of the polymers and reduced the domain sizes of the blends, resulting in increased J_{sc} and FF, thus enhancing the PCE.[36] In contrast, others pointed out that polymers with high M_n lead to coarser domains in BHJ films due to large liquid–liquid phase separations, which could cause increased charge recombination and suppressed charge extraction.[34] It seems that some contradictions appear. Moreover, the emerging class of acceptor polymers with conjugation breakers have not been well studied in terms of the impact of M_n on their photovoltaic performance.[37] To fully understand the issue, the transition from solution to solid-state should also be taken into consideration. It is a commonly accepted view that the drying process determines the final morphology on the micro/nano-scale level, such as the assembly of donor and acceptor molecules, the distribution of "pure" donor, acceptor, intermixed domains, and their domain sizes.[24,25] The pure domains govern the charge transportation behaviours,[38,39] and the intermixed amorphous part decides the charge separation efficiency.[40–42] The drying process can also affect the packing and alignment of polymer chains.[43,44]

Previously, to understand how the drying process impacts the blend morphology in organic solar cells, we studied the film formation processes of three representative BHJs composed of donor PBDB-T with acceptors $PC_{71}BM$, IT-M,

and N2200 by monitoring the drying process from liquids to films with *in situ* ultraviolet-visible (UV-vis) absorption spectra and photoluminescent (PL) spectroscopy.[45] The results indicate that higher molecular weight components dominate the drying process and final morphology of the BHJs. Furthermore, we investigated solvent impacts on the morphology of blend films and performance of the OSCs by monitoring the drying process of PBDBT:PF5–Y5 blends in chlorobenzene (CB) and *ortho*-xylene (*o*-XY) with *in situ* multifunctional spectroscopy.[46] Finer-mixed donor/acceptor nanostructures are obtained in CB-cast film corresponding to more efficient charge generation in the corresponding solar cells. In addition, we also revealed the function of a commonly used solvent additive 1-chloro-naphthalene (CN) in enhancing the performance of all-PSCs based on PBDB-T:PF5-Y5 by studying the drying process, which suggests that the improved performance of PBDB-T:PF5-Y5 solar cells originated from enhanced crystallinity and hole mobility since CN promotes self-aggregation of PBDB-T during the drying process.[47]

Recently, a kind of P_As with a flexible conjugation-break spacer (FCBS) has been developed. With the introduction of FCBS, the molecular rigidity and aggregation behavior of P_As could be regulated to achieve all-PSCs with improved mechanical properties and PV performance synergetically.[37,48] The reduced backbone rigidity helps improve the miscibility with P_Ds and extending the long-term stability of devices. Nevertheless, the effect of the molecular weight of these polymers on the morphology and performance in all-PSCs has not been explored, particularly its effects on crystallinity behavior and drying properties.

In this work, we systematically investigated the impact of the M_n of PYTS, a polymer acceptor with FCBS demonstrating a high PCE of 14.68% and excellent mechanical stretchability with a crack onset strain of 21.64% and toughness of 3.86 MJ m^{-3},[49] using PBDB-T (M_n = 35 kDa) as the polymer donor. Three PYTS polymers with different M_n were examined, including low M_n (~9 kDa), medium M_n (~13 kDa), and high M_n (~19 kDa), denoted as $PYTS_L$, $PYTS_M$, and $PYTS_H$, respectively. The devices based on $PYTS_H$ achieved the highest values of 9.43%, while those with $PYTS_L$ exhibited a significantly lower PCE of 5.99%. The morphological development in blends was monitored by *in situ* multi-spectroscopy, revealing that a blend consisting of $PYTS_H$ exhibits an extended drying time with the same material concentrations, resulting in more tightly packed structures with higher crystallinity, which are beneficial for more efficient charge carrier transport. Furthermore, with the help of transient absorption (TA), we found that the PBDB-T:$PYTS_H$ blend film shows a larger phase separation size and a longer lifetime of charge recombination, with which a higher possibility of charge extraction by electrodes can be reached. In summary, this study gives a cohesive comprehension regarding the influence of the polymer component molecular weight in all-PSCs on blend drying kinetics, charge transport characteristics, blend morphology, and photovoltaic characteristics, thereby establishing new correlations between molecular weight and device performance for more advanced all-PSC systems.

13030 | *J. Mater. Chem. C*, 2024, **12**, 13029–13039

This journal is © The Royal Society of Chemistry 2024

Experiment

Materials

All materials except the PYTS were purchased from commercial suppliers. PEDOT:PSS was purchased from Heraeus, and ZnO nanoparticles (NPs) were purchased from Avantama AG. The donor polymer PBDB-T was purchased from Ossila B.V. with a molar mass of M_n = 35 kDa and Đ = 2.2. PYTS was synthesized by Stille coupling reaction according to previously reported work.[49] Unless otherwise specified, such chemicals were used without any further purification.

Cyclic voltammetry

Cyclic voltammetry (CV) was measured to study the lowest unoccupied molecular orbital (LUMO) and highest occupied molecular orbital (HOMO) energy levels of the polymers. The samples drop-coated on the glassy carbon electrode were used as the working electrode. The counter electrode was platinum wire, and the reference electrode was an Ag/Ag$^+$ (0.01 M AgNO$_3$ + 0.1 M TBAPF$_6$) electrode. The electrolyte used in this work was acetonitrile containing 0.1 M TBAPF$_6$, at the scan rate of 50 mV s^{-1}.

In situ PL and absorption

The *in situ* PL setup is similar to our previous work.[45] In short, the polymer inks were coated on a pre-cleaned glass substrate using a blade coater (Erichsen 510) with a moving blade (ZFR 2040). A 532 nm continuous wave laser diode was used to excite the wet polymer films and an optical fiber was mounted on top of the resulting films, to continuously collect emission signals to the spectrometer (QE-Pro, Ocean Optics). The integration time for every PL spectrum was set to be 100 ms.

For the *in situ* absorption setup, a home-build stage was used to lift the glass substrate and the blade on top of the blade coater surface. An optical fiber was connected to a tungsten lamp (DH-2000, Ocean Optics) and mounted above the substrate, to shine white light onto the polymer films. The transmitted signals from the polymer films were guided by another optical fiber, which was mounted below the substrate, to the spectrometer. The integration time for every absorption spectrum was set to be 100 ms.

Transient absorption measurements

Femtosecond transient absorption measurements were carried out using a home-built transient absorption (TA) system. The light source of the TA system is a femtosecond laser coming from a regenerative amplifier (Legend Elite F 1K HE + II, Coherent), operating at 800 nm with a repetition rate of 1 kHz. The fundamental light is divided into two parts. One part of the light is used directly as the pump light. The other part is used to excite a sapphire plate for the generation of supercontinuum white light, which is further used as the probing light for differential absorption measurement. The probing light was guided into a monochromator (Omni-λ200i, Zolix) and detected using a CCD detector (Pascher Instrument). The pump "on" and "off" for a pair of sequential actinic pulses was regulated by a mechanical chopper (500 Hz, MC2000B-EC,

Thorlabs) in the pump beam. With the help of a mechanical delay line, the probe is time-delayed relative to the pump. The TA measurements were performed at room temperature in ambient air.

Atomic force microscopy

Atomic force microscopy (AFM) measurements were obtained using a Digital Instruments Dimension 3100 atomic force microscope operated in tapping mode, using a cantilever with a nominal spring constant of 40 N m^{-1}. The scan size was 1×1 µm. Samples were blade-coated with the CB solutions of PBDB-T:PYTS$_L$, PBDB-T:PYTS$_M$, and PBDB-T:PYTS$_H$ with 16 mg mL^{-1} (PBDB-T:PYTS = 1:1 weight ratio) on cleaned glass substrates at a speed of 11, 12, and 14 mm s^{-1}, respectively, under ambient conditions.

Grazing incident wide-angle X-ray scattering (GIWAXS)

The grazing incident wide-angle X-ray scattering (GIWAXS) measurements were performed at beamline 7.3.3 at the advanced light source. Samples were prepared on Si substrates using identical blend solutions as used in the devices. The 10 keV X-ray beam was incident at a grazing angle of 0.12° and 0.14°. The scattered X-ray was detected using a Dectris Pilatus 2 M photon counting detector.

Ellipsometry

Spectral Mueller matrices were recorded using a dual rotating compensator ellipsometer (RC2, J. A. Woollam Co., Inc.) in the spectral range 210–1690 nm at angles of incidences 45° to 75° in steps of 5°. Data analysis was performed using the CompleteEASE software (J. A. Woollam Co., Inc.). A measurement was done on a film-free glass sample and its refractive index was modeled with a Cauchy dispersion

$$n(\lambda) = A + \frac{B}{\lambda^2} + \frac{C}{\lambda^4},$$

where A, B and C are fit parameters. The backside of the glass substrate was roughened mechanically to reduce effects of backside reflections. The best fit $n(\lambda)$ spectrum was then used as the substrate refractive index for all samples with polymer films. For the polymer samples a three-phase model (substrate/film/ambient) was used. The film refractive index was fitted with non-linear regression using a Kramer–Kronig consistent B-spline dispersion model[50] simultaneously as the film thickness d was fitted. The thickness values reported have 90% confidence values of ±0.5 nm.

Device fabrication

Devices were fabricated with a structure of glass/indium tin oxide (ITO)/PEDOT:PSS/active layer/PFN-Br/Al. The glass/ITO substrate was first sonicated in DI water with detergent for 30 min, followed by cleaning with acetone and isopropyl alcohol (IPA) in an ultrasonic bath. This was followed by UV-ozone plasma for 20 min. PEDOT:PSS with a thickness of approximately 30 nm was deposited by spin-coating at 4000 rpm for 40 s. Later it was annealed in air for 20 min at 120 °C.

This journal is © The Royal Society of Chemistry 2024

J. Mater. Chem. C, 2024, **12**, 13029–13039 | **13031**

For spin-coating devices, after transferring substrates to a nitrogen glovebox, a first set of active layers were then spin-coated atop ITO/PEDOT:PSS from a solution of PBDB-T:PYTS$_L$, PBDB-T:PYTS$_M$, and PBDB-T:PYTS$_H$ with 16 mg mL^{-1} (PBDB-T:PYTS = 1:1 weight ratio) in CB, at 3500 rpm for 30 s. A second set of spin-coating devices from a solution of PBDB-T:PYTS$_L$, PBDB-T:PYTS$_M$, and PBDB-T:PYTS$_H$ with concentrations of 13 mg mL^{-1}, 16 mg mL^{-1}, and 19 mg mL^{-1} were made, with everything else alike. The samples were annealed at 120 °C for 10 min.

For blade-coating devices, the solution of PBDB-T:PYTS$_L$, PBDB-T:PYTS$_M$, and PBDB-T:PYTS$_H$ at a concentration of 16 mg mL^{-1} (PBDB-T:PYTS = 1:1 weight ratio) in CB was blade-coated atop the PEDOT:PSS layer at a speed of 11, 12, and 14 mm s^{-1} respectively under ambient conditions. Then, the samples were transferred into a glove box and annealed at 120 °C for 10 min under nitrogen. The thicknesses of the active layer were optimized between 85 and 105 nm.

Later, deposition of PFN-Br (0.5 mg mL^{-1} in methanol) was completed at 4000 rpm for 30 s atop the active layer. Finally, the top Al electrode of 100 nm thickness was thermally evaporated through a mask with a background pressure of $\sim 2 \times 10^{-7}$ mbar. The areas of the all-PSCs are about 0.04 cm^2. The devices were encapsulated using glass and epoxy adhesive before removal from the glove box for measurements.

Characterization

The current density–voltage (J–V) characteristics of the solar cells were measured using a Keithley 2400 source meter unit under AM1.5G (100 mW cm^{-2}) irradiation from a solar simulator (Newport MiniSol™ model LSH-7320). The J–V curves were measured from −2 to 2 V. The scan speed and dwell times were fixed at 0.05 V per step and 2 ms, respectively. The EQE spectra were measured using a QE-R solar cell spectral response measurement system (Enli Technology Co., Ltd, Taiwan).

Space-charge limited current (SCLC) measurement

The electron and hole mobilities of BHJ films were measured by using the method of SCLC. The electron-only device with an architecture of ITO/ZnO nanoparticles (NPs)/PFN-Br/PBDB-T:PYTS/LiF/Al and the hole-only device with an architecture of ITO/PEDOT:PSS/PBDB-T:PYTS/MoO$_x$/Al were fabricated. The mobility was determined by fitting the dark current to the model of a single carrier SCLC, described by the equation:

$$J = \frac{9\varepsilon_0 \varepsilon_r \mu V^2}{8L^3},$$

where J is the current density, ε_0 is the permittivity of free space, ε_r is the relative dielectric constant of the transport medium, μ is the charge mobility and L is the thickness of the active layer. $V = V_{app} - V_{bi}$, where V_{app} is the applied voltage, and V_{bi} is the offset voltage. The mobility can be calculated from the slope of the $J^{0.5} \sim V$ curves.

Results and discussion

Electrochemical and optical properties

The chemical structures of PBDB-T and PYTS are shown in Fig. 1a. The molecular weight and polydispersity index of the PYTS samples were characterized by gel permeation
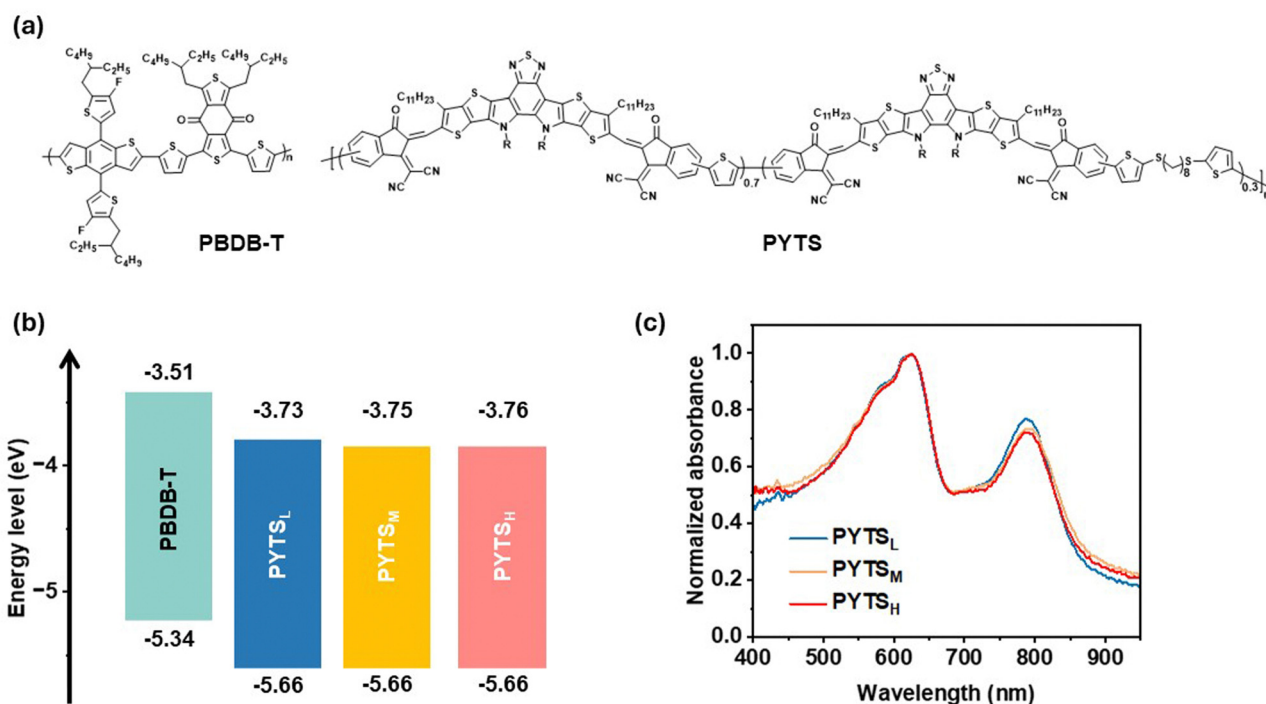

Fig. 1 (a) Molecular structures of donor polymer (PBDB-T) and acceptor polymer (PYTS). (b) HOMO/LUMO energy levels of the acceptor polymer of varying M_n. (c) Thin-film optical absorption spectra of the PBDB-T:PYTS blend films, with different M_n of PYTS polymers.

Table 1 Molecular weight, optical properties, and electronic properties of PYTS P_As

P_As	M_n (kDa)	M_w (kDa)	PDI	λ_{max} (nm)	E_g (eV)	E_{HOMO} (eV)	E_{LUMO} (eV)
$PYTS_L$	9	25	2.7	787	1.4	−5.66	−3.73
$PYTS_M$	13	37	2.9	791	1.4	−5.66	−3.75
$PYTS_H$	19	99	5.1	791	1.4	−5.66	−3.76

chromatography (GPC). The data are summarized in Fig. S1 (ESI†) and Table 1. The energy levels of PBDB-T and PYTS series were calculated using CV (Fig. S2, ESI†), as shown in Fig. 1b. The LUMO and HOMO energy levels of PYTS with different M_n only have a tiny gap (Table 1), suggesting the M_n has little impact on energy levels, as expected due to their similarity in chemical composition.

Three polymer acceptors $PYTS_L$, $PYTS_M$, and $PYTS_H$ were characterized for their optical properties as blend films with PBDB-T. The UV-vis absorption spectra measured in films are shown in Fig. 1c, and the corresponding data are summarized in Table 1. In the films, as M_n increased, the absorption maximum (λ_{max}) showed a red shift from 787 nm of $PYTS_L$ to 791 nm of $PYTS_H$, while the λ_{max} of $PYTS_M$ remained consistent with $PYTS_H$, suggesting that $PYTS_H$ and $PYTS_M$ demonstrated stronger π–π interactions compared to $PYTS_L$.

The ellipsometer was used to measure the refractive index (n) and extinction coefficient (k) values of three PYTS acceptors. As shown in Fig. S3 (ESI†), all the blend films show similar n and k values and show an absorption onset at 1.4 eV, with contributions from both the donor and the acceptor. It indicated that the M_n has little impact on the optical bandgap of this semiconductor, consistent with the absorption results.

Photovoltaic performance

To explore the influence of the PYTS series with different M_n on the photovoltaic performance, all-PSCs with a regular structure of ITO/PEDOT:PSS/PBDB-T:PYTS/PFN-Br/Al were fabricated *via* blade-coating. The detailed procedures for the device fabrication are described in the experimental section. The devices with the same concentration of 16 mg mL^{-1} were fabricated *via* spin-coating. The distributions of open circuit voltage (V_{oc}), J_{sc}, FF and PCE were depicted in Fig. S4 (ESI†) and the photovoltaic parameters are listed in Table S1 (ESI†). In comparison to devices based on $PYTS_L$, those based on $PYTS_M$ and $PYTS_H$ have attained a much higher efficiency, where the optimal device reaches maximum PCEs of 8.16% and 8.14%, respectively, accompanied by synergistic enhancements in V_{oc}, J_{sc}, and FF. However, it was observed that the same concentration for blends with different M_n gives different viscosity of the active layer solution. Specifically, a higher molecular weight results in greater solution viscosity, which not only directly influences the film formation dynamics and morphology during spin coating, but also leads to a thicker active layer. Different viscosity leads to different layer thicknesses, which may not be the optimized conditions for each device. The thickness-dependent performance of all-PSCs is shown in

Fig. S5 (ESI†). In addition, viscosity influences the competitive relationship between solid–liquid (S–L) demixing and liquid–liquid (L–L) demixing. Lower solution viscosity would extend the polymer crystal growth time, contributing to increased coarseness. Conversely, increased viscosity prevents large-scale L–L phase separation.[24,51] To optimize the device performance, we used different material concentrations for controlled solution viscosity for device fabrication and the detailed photovoltaic performance of the investigated PBDB-T:PYTS all-PSCs are shown in Fig. S6 (ESI†). Additionally, Fig. 2a plots the J–V curves of the best-performing solar cells based on the PYTS series as acceptors, with corresponding photovoltaic parameters summarized in Table 2. All-PSCs based on PBDB-T:$PYTS_H$ exhibit the highest PCE of 9.43% with a V_{oc} of 0.90 V, a J_{sc} of 18.55 mA cm^{-2}, and an FF of 56.32%. Slightly lower performance is found for the PBDB-T:$PYTS_M$ devices with a PCE of 8.16%, accompanied by a V_{oc} of 0.90 V, a J_{sc} of 17.10 mA cm^{-2}, and an FF of 53.30%. However, a much lower PCE of 5.99% with a V_{oc} of 0.89 V, a J_{sc} of 13.02 mA cm^{-2}, and an FF of 51.57% was obtained for the PBDB-T:$PYTS_L$ devices, mainly due to the drastically reduced J_{sc} and FF values. The external quantum efficiency (EQE) results demonstrated an increased photon response in the entire absorption range (Fig. 2b), which is consistent with the improved J_{sc} values for the corresponding $PYTS_H$-based devices. Furthermore, the all-PSCs *via* blade-coating were fabricated as well, using different blade moving speeds to achieve optimized thicknesses. It yields similar trends in variation, with relevant photovoltaic parameters provided in the ESI† (Fig. S7 and Table S2). Impressively, the dark-current values systematically decreased with increasing M_n of P_As, which indicated PBDB-T:$PYTS_H$ all-PSCs possessed increased shunt resistance and suppressed leakage current, compared to those of $PYTS_L$- and $PYTS_M$-based devices (Fig. 2c).

To gain a deeper insight into the FF and J_{sc} changes between devices, the charge mobilities for blends were evaluated by the space charge limited current (SCLC) method (Fig. 2d and Fig. S8, ESI†). The hole mobilities (μ_hs), which were estimated from hole-only devices with a structure of ITO/PEDOT:PSS/PBDB-T:PYTS/MoO$_x$/Al, are 5.78×10^{-4} cm^2 V^{-1} s^{-1} (PBDB-T:$PYTS_L$), 5.92×10^{-4} cm^2 V^{-1} s^{-1} (PBDB-T:$PYTS_M$) and 5.89×10^{-4} cm^2 V^{-1} s^{-1} (PBDB-T:$PYTS_H$), respectively. The μ_h remains independently unchanged in different blend films due to the same donor. The μ_es from electron-only devices of ITO/ZnO NPs/PFN-Br/PBDB-T:PYTS/LiF/Al were 7.91×10^{-5} cm^2 V^{-1} s^{-1} (PBDB-T:$PYTS_L$), 9.97×10^{-5} cm^2 V^{-1} s^{-1} (PBDB-T:$PYTS_M$) and 1.67×10^{-4} cm^2 V^{-1} s^{-1} (PBDB-T:$PYTS_H$), respectively. The improved electron mobilities of PBDB-T:$PYTS_H$, which could be ascribed to the enhanced crystallinity of the acceptor, balance the charge transport of blends, presenting a minimum μ_h/μ_e value of 3.52, while that of PBDB-T: $PYTS_L$ and PBDB-T:$PYTS_M$ are 5.94 and 7.30, respectively. The enhancement of charge carrier transport property allowed the $PYTS_H$-based devices to achieve an improved J_{sc} and FF. It is well recognized that FF mainly depends on free charge recombination and charge carrier transport. We noticed that the devices processed active
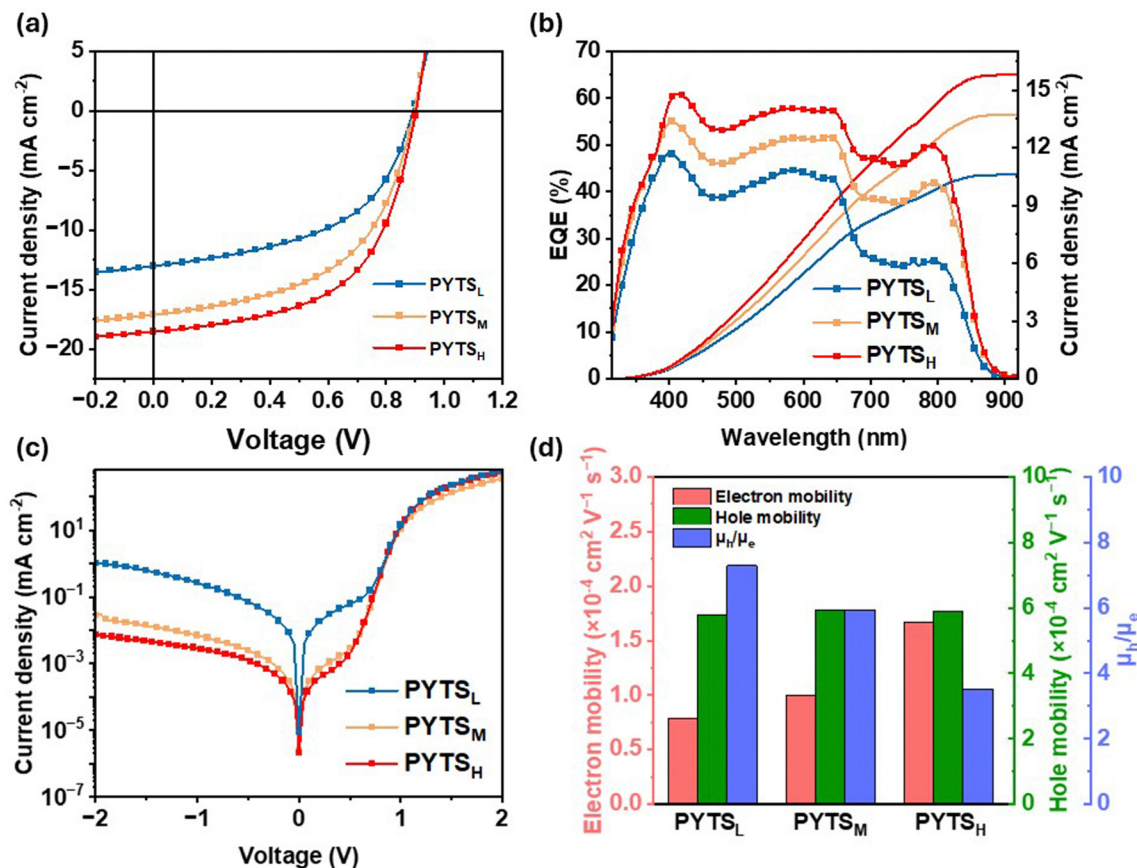
Fig. 2 The PYTS M_n dependence of photovoltaic properties of optimized PBDB-T:PYTS devices. (a) J–V curves, (b) EQE spectra, (c) dark J–V curves and (d) charge mobilities.

Table 2 PV performances of the all-PSCs vs. the M_n of P_As

	V_{oc} (V)	J_{sc} (mA cm^{-2})	FF (%)	PCE[a] (%)
PBDB-T:PYTS$_L$	0.89 (0.88 ± 0.008)	13.02 (11.59 ± 0.67)	51.57 (49.84 ± 5.48)	5.99 (5.10 ± 0.75)
PBDB-T:PYTS$_M$	0.90 (0.89 ± 0.004)	17.10 (15.60 ± 1.17)	53.30 (53.79 ± 2.58)	8.16 (7.64 ± 0.39)
PBDB-T:PYTS$_H$	0.90 (0.89 ± 0.010)	18.55 (16.73 ± 1.25)	56.32 (57.57 ± 1.75)	9.43 (8.60 ± 0.63)

[a] The values in parenthesis are the standard deviation obtained from 24 devices.

layers from solutions at RT exhibit relatively smaller FFs than those of all-PSCs based on PBDB-T:PYTS$_M$ spin-coated from hot solutions at 80 °C.[49] By comparing the above electron mobilities (from 7.91×10^{-5} cm^2 V^{-1} s^{-1} to 1.67×10^{-4} cm^2 V^{-1} s^{-1}) with those (4.8×10^{-4} cm^2 V^{-1} s^{-1}) in ref. 49, we believe that the smaller FFs in our devices could be dominantly attributed to the relatively smaller μ_es of PYTS acceptors and their imbalance with the μ_h ($\sim 5.8 \times 10^{-4}$ cm^2 V^{-1} s^{-1}) of the donor PBDB-T. Slowly electron transport from the BHJs to the collecting electrode would increase the possibility of charge recombination and reduce FFs.

We further evaluated the correlation between M_n and the storage stability of all-PSCs. As shown in Fig. S9 (ESI†), all devices exhibit two stage degradations, a fast decay in 72 hours, then followed by a slow decay. The stabilities present an opposite tendence with device performance and M_n, that is,

the PYTS$_L$-based devices showed the best stability, remaining 72.7% of the initial PCE after 288 hours, while PYTS$_M$ and PYTS$_H$-based devices decayed to 64.4% and 60.4% of the initial PCE, respectively. The stability result suggests that a higher M_n of PYTS acceptors could not enhance the stability of all-PCSs.

In situ monitoring of film-formation and morphology development

Fully comprehending and regulating morphology can be obtained by monitoring the film formation process of BHJ films. In this study, we used in situ UV-vis and PL spectroscopic recording film drying through blade-coating with a custom-built setup[45] to discern the effects of the molecular weight of P_As on morphological evolution.[46,47] Fig. S10 (ESI†) depicts the temporal evolutions of UV-vis absorption contour maps of blends with P_As of different M_n, where the colors represent

13034 | J. Mater. Chem. C, 2024, 12, 13029–13039

This journal is © The Royal Society of Chemistry 2024

the intensity of absorption signals at a specific time interval and wavelength. According to our previous work, the drying process can be divided into three temporal stages, *i.e.*, the liquid film stage ($t0 < t < t1$), the liquid–solid transition stage ($t1 < t < t2$), and eventually the dried film stage ($t2 < t$).[47] As seen in Fig. S11 (ESI†), the absorption peaks of PYTS in all blend films present different degrees of red shifts (from 773 nm to 788 nm for $PYTS_L$, from 776 nm to 787 nm for $PYTS_M$, and from 776 nm to 782 nm for $PYTS_H$), implying the presence of ordered packing in these molecules and the formation of π–π interactions in the solid films. After annealing, the peak positions of $PYTS_M$ and $PYTS_H$ exhibit a further red-shift to 791 nm (Fig. S12, ESI†), which is attributed to the further aggregation of the longer polymer chains under thermal stress. In the meantime, the peak position of PBDB-T remained almost unchanged along with time in all three systems (~620 nm). In our previous work, a similar phenomenon was observed. This indicates that self-aggregation of PBDB-T was restricted by blending with polymer acceptors.[29,31] By increasing M_n, the crystallization of the blend film tended to slow down, as revealed by the extended drying time from 33 s ($PYTS_L$), to 43 s ($PYTS_M$) and to 51 s ($PYTS_H$) (Fig. S11, ESI†). With longer crystallization time, the crystal size could be larger, forming more ordered crystallinity structures. These behaviors are in line with the observation that the film morphology of the blends containing $PYTS_H$ exhibits strongest crystalline order shown in GIWAXS measurements, compared to that of $PYTS_L$, which will be discussed later.

We proceeded to assess the quenching kinetics through *in situ* PL characterization. The contour maps demonstrating PL evolution are presented in Fig. S13 (ESI†). Fig. 3 displays the time-dependent PL peak location and intensity of blends consisting of P_AS with different M_n. The extracted temporal evolutions of the PL peak position and integrated intensity are associated with the spatial distribution of fluorophores and quenchers in the blends.[52] The PL peak position exhibited a similar evolution trend to that observed in the *in situ* absorption spectra, characterizing three stages as well. Within the liquid film stage, the emission from PYTS undergoes a gradual quenching with a weak red shift, indicating the slight enhancement of interactions between polymer chains. Besides, compared to $PYTS_L$, $PYTS_M$ and $PYTS_H$ show a greater redshift of the original PL peak, implying stronger preaggregation of acceptors in solutions. The PBDB-T:$PYTS_L$ blend film shows a liquid film stage time of 12 s, which is much shorter than that of PBDB-T:$PYTS_M$ (21 s) and PBDB-T:$PYTS_H$ (24 s). It indicates a more rapid formation of interactions between PBDB-T and $PYTS_L$, accelerating the growth rate of the film. In the second stage, the PYTS shows a more rapid quenching, accompanied by a rapid red shift. The spectral red-shift contributes to the polymer aggregation and the rapid drops in the PL signals arise from the fluorophore-quencher interaction.[53] This suggested the proximity between the donor and acceptor molecules decreases as the solvent evaporates. Compared with the PBDB-T:$PYTS_L$ blend film ($t2 \sim 17$ s), the prolonged PL quenching of PBDB-T:$PYTS_H$ ($t2 \sim 30$ s) can be assigned to a slower interdiffusion process
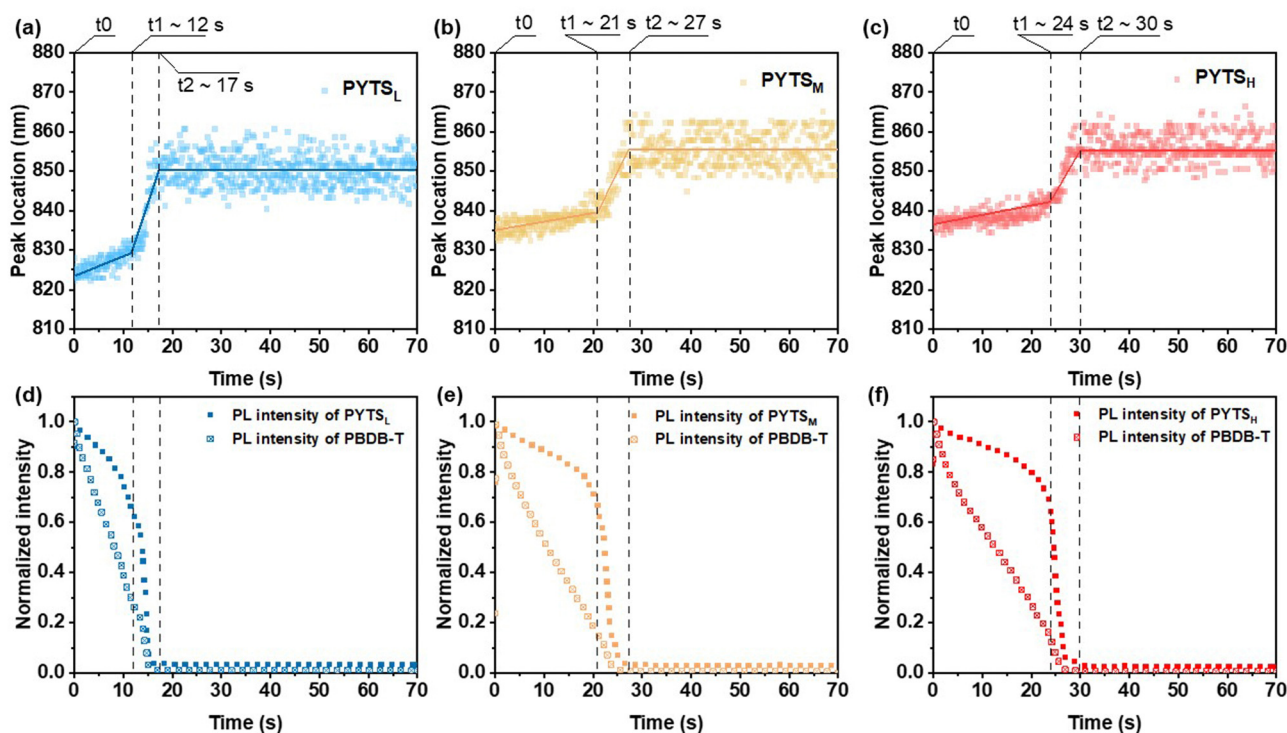

Fig. 3 *In situ* PL results of the PBDB-T:PYTS blend film *via* blade-coating, as a function of drying time. Locations of emission peaks of (a) $PYTS_L$, (b) $PYTS_M$, and (c) $PYTS_H$, respectively. Peak intensity for PBDB-T and PYTS emission peaks (at 670 and 850 nm, respectively) of (d) $PYTS_L$, (e) $PYTS_M$, and (f) $PYTS_H$, respectively.

between PBDB-T and PYTS$_H$, implying a lower miscibility between these two polymers. Therefore, a larger phase separation was formed in the PBDB-T:PYTS$_H$ film. With the larger pure phase of donor and acceptor, the charge carrier transportation can be enhanced, in line with the improved mobility values. After that, the PL intensities and peak positions are constant, suggesting the complete formation of solid films.

TA spectroscopy

To investigate the role of molecular weight on charge photo-generation and recombination processes in an ultrafast timescale, we performed the transient absorption (TA) measurements of blend films. Fig. 4 shows the TA spectra of the blend films at the indicated delay time by selecting to excite the acceptor materials with the excitation wavelength of 800 nm.

The TA kinetics of ~645 nm were extracted to estimate the charge photogeneration and recombination processes in the blend films, which corresponds to the ground state bleaching process of the donor material, as shown in Fig. S14 (ESI†). The kinetics of 645 nm in the PBDB-T:PYTS$_L$ blend film display a fast generation and a slow relaxation process. However, an instantaneous generation, a slow rise and a slow relaxation process is exhibited in the kinetics of ~645 nm in PBDB-T:PYTS$_M$ and PBDB-T:PYTS$_H$ blend films. The dynamics of hole-transfer involve both an ultrafast charge-transfer process and an exciton diffusion-mediated charge transfer process, that can be fitted by a biexponential function:[46,54]

$$I = A_1\left(1 - \exp\left(-\frac{t}{\tau_1}\right)\right) + A_1\left(1 - \exp\left(-\frac{t}{\tau_2}\right)\right),$$

where τ_1 represents the lifetime of the fast hole transfer process at the interface and τ_2 is the lifetime of exciton-diffusion-mediated hole transfer determined by the domain size. In general, a longer exciton-diffusion-mediated lifetime indicates a larger phase-separated size between donor and acceptor in blend films. From the fitting results, shown in Table S3 (ESI†), the three blend films show comparable ultrafast charge transfer, however, the PBDB-T:PYTS$_H$ blend film exhibits a longer exciton diffusion time of ≈12.3 ps than PBDB-T:PYTS$_M$ (≈5.7 ps) and PBDB-T:PYTS$_L$ (within instrument response

function), indicating a larger acceptor domain size in PBDB-T:PYTS$_H$ films.[55–57] The phase domain size increases with the increasing molecular weight of P$_A$, which corresponds with the results of AFM measurements (Fig. S16, ESI†).

Besides, we found the TA kinetics of 645 nm recovered with a delay time longer than 30 ps, which can be attributed to the charge recombination process. Accordingly, the charge recombination rate is independent and dependent on the excitation fluency in geminate recombination and bimolecular recombination, respectively. In this work, we performed the TA measurements of blend films with different fluencies, as shown in Fig. S15 (ESI†). It can be seen that the charge recombination mechanism for PBDB-T:PYTS$_L$, PBDB-T:PYTS$_M$ and PBDB-T:PYTS$_H$ blend films can be attributed to geminate, geminate, and bimolecular recombination, respectively. Besides, by using the single-exponential function to fit the charge recombination kinetics of 645 nm, we can estimate the lifetime of charge recombination to ~3.7 ns, ~3.9 ns, and ~5.4 ns for PBDB-T:PYTS$_L$, PBDB-T:PYTS$_M$ and PBDB-T:PYTS$_H$ blend films, respectively, and the detailed fitting parameters can be found in Table S4 (ESI†). This indicates the increasing molecular weight of the acceptor material can suppress the charge recombination process in the blend film. Combining the TA measurement and the performance of devices, it is concluded that the PBDB-T:PYTS$_H$ blend film shows a larger acceptor phase separation, a longer lifetime of charge recombination and thus a higher PCE of ~9.43% over those of PBDB-T:PYTS$_L$ blend film, indicating the M_n plays a critical role in charge transportation and recombination processes and the performance of devices.

Morphological properties

To elucidate the origins of the different photovoltaic performance of the PBDB-T:PYTS blends, we examined the morphological properties of the blend films using the combined measurements of grazing incident wide-angle X-ray diffraction (GIWAXS) and atomic force microscopy (AFM). In the AFM images, as M_n increased from 9 kDa to 19 kDa, the root-mean-square averaged surface roughness (R_q) of the blends increased from 1.24 nm to 1.75 nm (Fig. S16, ESI†), and the sizes of the domains
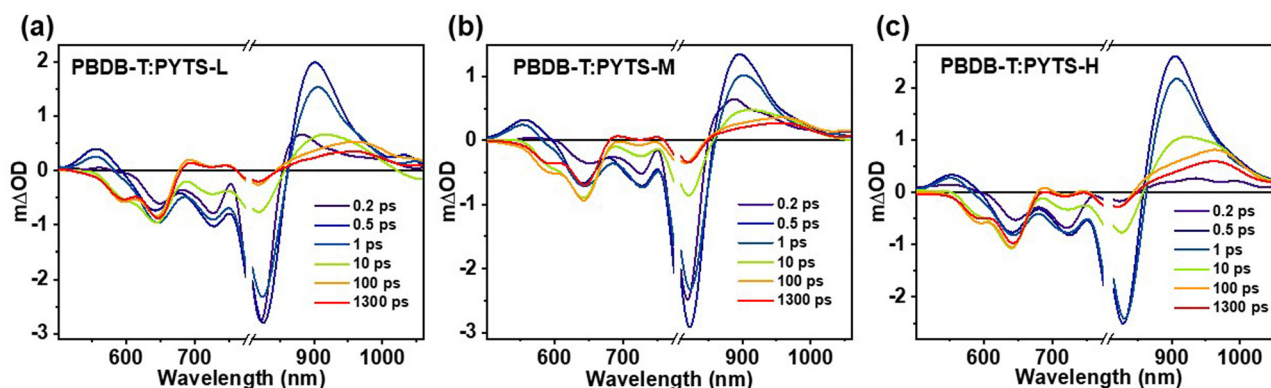

Fig. 4 The representative TA spectra of (a) PBDB–T:PYTS$_L$, (b) PBDB–T:PYTS$_M$ and (c) PBDB–T:PYTS$_H$ blend films after excitation at 800 nm with an excitation fluence of 3.6×10^{13} photons cm^{-2} pulse^{-1}.

13036 | *J. Mater. Chem. C*, 2024, **12**, 13029–13039

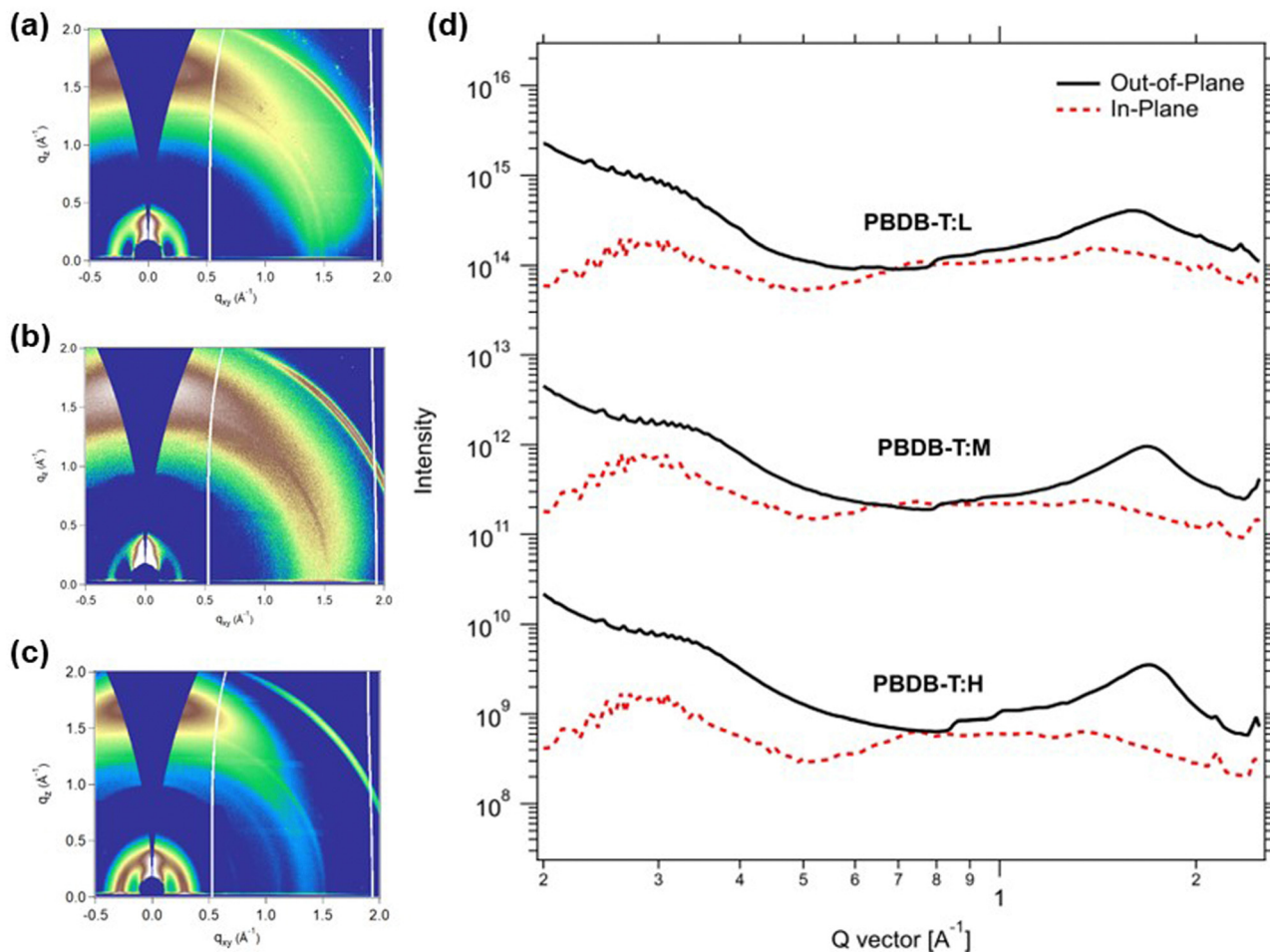This journal is © The Royal Society of Chemistry 2024

Fig. 5   2D GIWAXS patterns of PBDB-T:PYTS blend films with different M_n. (a) PBDB-T:PYTS$_L$, (b) PBDB-T:PYTS$_M$, and (c) PBDB-T:PYTS$_H$. (d) Linecuts of GIWAXS patterns for the three blend films.

became larger with increasing M_n. This indicates that the longer polymer chains increased the phase segregation degree between P_D and P_A. The PBDB-T:PYTS$_L$ films lack phase separated domains, which suppressed the exciton dissociation and promoted charge recombination, thus resulting in reduced J_{sc} and FF. Fig. 5a–c presents the 2D GIWAXS images of PBDB-T:PYTS blends, with Fig. 5d showing the 1D scattering profiles of the blends taken along the in-plane and out of plane directions. Table S5 (ESI†) presents the peak fitting results for the out-of-plane π stacking peaks (010) and in-plane (100) peaks in the blends. The PBDB-T:PYTS$_L$ blend film shows a broad (010) peak in the out-of-plane (OOP) direction at 1.66 Å^{-1} (d = 3.78 Å) with a crystal coherence length (CCL) of 1.61 nm and a (100) peak in the in-plane (IP) direction at 0.28 Å^{-1} (d = 22.44 Å) with a CCL of 7.84 nm. The PBDB-T:PYTS$_M$ and PBDB-T:PYTS$_H$ blend film exhibits enhanced molecular co-facial packing, as indicated by the sharper (010) peak in the OOP direction at 1.68 Å^{-1} (d = 3.74 Å) with an increased CCL of 1.77 and 2.19 nm, respectively, indicating the π–π stacking and crystal size of polymers were further improved. Generally, the π–π stacking distance and CCL results affect the charge transport characteristics of the polymer materials.[39,58] By increasing M_n, the blends utilize a better transport feature of PYTS$_H$ than PYTS$_L$

due to larger pure polymer domains, which is consistent with the mobility values.

Conclusions

In this work, from liquids to films and devices, the M_n effect of PYTS on PCEs of all-PSCs based on PBDB-T:PYTS blends with three different M_n has been comprehensively investigated using *in situ* spectroscopy and several *ex situ* techniques. The J_{sc} of devices increases with the M_n (9, 13 and 19 kDa) of PYTS from 13.02, 17.16 to 18.73 mA cm^{-2}, which results in PCE enhancement from 5.99%, 8.16% to 9.43%. The morphology evolutions from liquids to solid BHJs of the three PBDB-T:PYTS systems were monitored using *in situ* multifunctional spectroscopy. Furthermore, the nanostructures of PBDB-T:PYTS films, charge generation, transport and recombination of corresponding all-PSCs were characterized with GIWAXS, AFM and TAS. The results indicate that the increased PCE of all-PSCs with M_n of PYTS was mainly attributed to the improved crystallinity in PBDB-T:PYTS$_H$ during drying, which facilitates electron transport, prolongs carrier lifetimes and decreases the non-geminate

This journal is © The Royal Society of Chemistry 2024

J. Mater. Chem. C, 2024, **12**, 13029–13039 | **13037**

recombination rate constants. This study deepens our understanding of the interplay between M_n, morphology evolutions, nanostructure of BHJs, and the photovoltaic performance in the corresponding devices. It also highlights the irreplaceable function of *in situ* spectroscopy to record the nanostructure evolution from liquid to BHJ for further improving the PCEs of full PSCs.

Author contributions

Y. L. conceived the topic and guided S. E. on the *in situ* setup. J. X. and S. E. conducted the experiments of *in situ* analysis, fabrication and characterization of all-PSCs. Z. G. and E. W. provided polymer acceptors. G. W. and W. Z. conducted and analysed TA measurement, R. Z. carried out GIWAXS and interpretation. L. Q. took voltammetry measurements. L. W. imaged the surfaces of blend films with AFM, Y. L. and N. Y. assistant S. E. work in the lab, J. X. and F. Z. composed the draft of the manuscript, integrated contributions from all co-authors and finalized the manuscript. F. Z. supervised the work and coordinated the collaborations.

Data availability

The data supporting this article have been included as part of the ESI.†

Conflicts of interest

There are no conflicts to declare.

Acknowledgements

Notes and references

1 J. J. M. Halls, C. A. Walsh, N. C. Greenham, E. A. Marseglia, R. H. Friend, S. C. Moratti and A. B. Holmes, *Nature*, 1995, **376**, 498–500.
2 G. Yu and A. J. Heeger, *J. Appl. Phys.*, 1995, **78**, 4510–4515.
3 M. Jonforsen, T. Johansson, O. Inganäs and M. R. Andersson, *Macromolecules*, 2002, **35**, 1638–1643.
4 F. Zhang, M. Jonforsen, D. M. Johansson, M. R. Andersson and O. Inganäs, *Synth. Met.*, 2003, **138**, 555–560.
5 M. Granström, K. Petritsch, A. C. Arias, A. Lux, M. R. Andersson and R. H. Friend, *Nature*, 1998, **395**, 257–260.
6 A. C. Arias, J. D. MacKenzie, R. Stevenson, J. J. M. Halls, M. Inbasekaran, E. P. Woo, D. Richards and R. H. Friend, *Macromolecules*, 2001, **34**, 6005–6013.
7 C. J. Brabec, N. S. Sariciftci and J. C. Hummelen, *Adv. Funct. Mater.*, 2001, **11**, 15–26.
8 J. Yi, G. Zhang, H. Yu and H. Yan, *Nat. Rev. Mater.*, 2024, **9**, 46–62.
9 H. Yu, Y. Wang, X. Zou, J. Yin, X. Shi, Y. Li, H. Zhao, L. Wang, H. M. Ng, B. Zou, X. Lu, K. S. Wong, W. Ma, Z. Zhu, H. Yan and S. Chen, *Nat. Commun.*, 2023, **14**, 2323.
10 C. Lee, S. Lee, G.-U. Kim, W. Lee and B. J. Kim, *Chem. Rev.*, 2019, **119**, 8028–8086.
11 G. Wang, F. S. Melkonyan, A. Facchetti and T. J. Marks, *Angew. Chem., Int. Ed.*, 2019, **58**, 4129–4142.
12 Z. Genene, W. Mammo, E. Wang and M. R. Andersson, *Adv. Mater.*, 2019, **31**, 1807275.
13 Q. Fan, W. Su, S. Chen, W. Kim, X. Chen, B. Lee, T. Liu, U. A. Méndez-Romero, R. Ma, T. Yang, W. Zhuang, Y. Li, Y. Li, T.-S. Kim, L. Hou, C. Yang, H. Yan, D. Yu and E. Wang, *Joule*, 2020, **4**, 658–672.
14 R. Zeng, L. Zhu, M. Zhang, W. Zhong, G. Zhou, J. Zhuang, T. Hao, Z. Zhou, L. Zhou, N. Hartmann, X. Xue, H. Jing, F. Han, Y. Bai, H. Wu, Z. Tang, Y. Zou, H. Zhu, C.-C. Chen, Y. Zhang and F. Liu, *Nat. Commun.*, 2023, **14**, 4148.
15 P. Wu, Y. Duan, Y. Li, X. Xu, R. Li, L. Yu and Q. Peng, *Adv. Mater.*, 2024, **36**, 2306990.
16 T. Zhang, Y. Xu, H. Yao, J. Zhang, P. Bi, Z. Chen, J. Wang, Y. Cui, L. Ma, K. Xian, Z. Li, X. Hao, Z. Wei and J. Hou, *Energy Environ. Sci.*, 2023, **16**, 1581–1589.
17 Z. Ge, J. Qiao, Y. Li, J. Song, C. Zhang, Z. Fu, M. H. Jee, X. Hao, H. Y. Woo and Y. Sun, *Adv. Mater.*, 2023, **35**, 2301906.
18 J. Wen, R. Lin, Y. Wu, H. Zhang, H. Zhou, Z. Liu, Y. Xie, D. Ye and X. Ouyang, *EcoMat*, 2023, **5**, e12318.
19 J. Xiang, Z.-X. Liu, H. Chen and C.-Z. Li, *Adv. Mater.*, 2023, **35**, 2303729.
20 J. Wen, R. Lin, Y. Wu, H.-C. Hu, Z. Liu, H. Zhou and X. Ouyang, *Chem. Eng. J.*, 2022, **450**, 138169.
21 Z.-G. Zhang and Y. Li, *Angew. Chem., Int. Ed.*, 2021, **60**, 4422–4433.
22 D. Mori, H. Benten, H. Ohkita and S. Ito, *Adv. Energy Mater.*, 2015, **5**, 1500304.
23 R. S. Gurney, D. G. Lidzey and T. Wang, *Rep. Prog. Phys.*, 2019, **82**, 036601.

13038 | *J. Mater. Chem. C*, 2024, **12**, 13029–13039

This journal is © The Royal Society of Chemistry 2024

24 C. McDowell, M. Abdelsamie, M. F. Toney and G. C. Bazan, *Adv. Mater.*, 2018, **30**, 1707114.

25 N. D. Treat and M. L. Chabinyc, *Annu. Rev. Phys. Chem.*, 2014, **65**, 59–81.

26 J. Wang, Y. Wang, K. Xian, J. Qiao, Z. Chen, P. Bi, T. Zhang, Z. Zheng, X. Hao, L. Ye, S. Zhang and J. Hou, *Adv. Mater.*, 2024, **36**, 2305424.

27 J. J. van Franeker, G. H. L. Heintges, C. Schaefer, G. Portale, W. Li, M. M. Wienk, P. van der Schoot and R. A. J. Janssen, *J. Am. Chem. Soc.*, 2015, **137**, 11783–11794.

28 A. Khasbaatar, Z. Xu, J.-H. Lee, G. Campillo-Alvarado, C. Hwang, B. N. Onusaitis and Y. Diao, *Chem. Rev.*, 2023, **123**, 8395–8487.

29 Q. Fan, Q. An, Y. Lin, Y. Xia, Q. Li, M. Zhang, W. Su, W. Peng, C. Zhang, F. Liu, L. Hou, W. Zhu, D. Yu, M. Xiao, E. Moons, F. Zhang, T. D. Anthopoulos, O. Inganäs and E. Wang, *Energy Environ. Sci.*, 2020, **13**, 5017–5027.

30 K. Zhou, K. Xian and L. Ye, *InfoMat*, 2022, **4**, e12270.

31 Z. Wang, Y. Guo, X. Liu, W. Shu, G. Han, K. Ding, S. Mukherjee, N. Zhang, H.-L. Yip, Y. Yi, H. Ade and P. C. Y. Chow, *Nat. Commun.*, 2024, **15**, 1212.

32 D. K. Tran, I. Robitaille, I. Jo Hai, X. Ding, D. Kuzuhara, T. Koganezawa, Y.-C. Chiu, M. Leclerc and S. A. Jenekhe, *J. Mater. Chem. A*, 2020, **8**, 21070–21083.

33 N. Zhou, A. S. Dudnik, T. I. N. G. Li, E. F. Manley, T. J. Aldrich, P. Guo, H.-C. Liao, Z. Chen, L. X. Chen, R. P. H. Chang, A. Facchetti, M. Olvera de la Cruz and T. J. Marks, *J. Am. Chem. Soc.*, 2016, **138**, 1240–1251.

34 K. D. Deshmukh, R. Matsidik, S. K. K. Prasad, L. A. Connal, A. C. Y. Liu, E. Gann, L. Thomsen, J. M. Hodgkiss, M. Sommer and C. R. McNeill, *Adv. Funct. Mater.*, 2018, **28**, 1707185.

35 Z. Li, W. Zhong, L. Ying, F. Liu, N. Li, F. Huang and Y. Cao, *Nano Energy*, 2019, **64**, 103931.

36 H. Kang, M. A. Uddin, C. Lee, K.-H. Kim, T. L. Nguyen, W. Lee, Y. Li, C. Wang, H. Y. Woo and B. J. Kim, *J. Am. Chem. Soc.*, 2015, **137**, 2359–2365.

37 Q. Fan, W. Su, S. Chen, T. Liu, W. Zhuang, R. Ma, X. Wen, Z. Yin, Z. Luo, X. Guo, L. Hou, K. Moth-Poulsen, Y. Li, Z. Zhang, C. Yang, D. Yu, H. Yan, M. Zhang and E. Wang, *Angew. Chem., Int. Ed.*, 2020, **132**, 20007–20012.

38 S. Fratini, M. Nikolka, A. Salleo, G. Schweicher and H. Sirringhaus, *Nat. Mater.*, 2020, **19**, 491–502.

39 K. Gu and Y.-L. Loo, *J. Polym. Sci., Part B: Polym. Phys.*, 2019, **57**, 1559–1571.

40 A. J. Gillett, A. Privitera, R. Dilmurat, A. Karki, D. Qian, A. Pershin, G. Londi, W. K. Myers, J. Lee, J. Yuan, S.-J. Ko, M. K. Riede, F. Gao, G. C. Bazan, A. Rao, T.-Q. Nguyen, D. Beljonne and R. H. Friend, *Nature*, 2021, **597**, 666–671.

41 K. Gu, C. R. Snyder, J. Onorato, C. K. Luscombe, A. W. Bosse and Y.-L. Loo, *ACS Macro Lett.*, 2018, **7**, 1333–1338.

42 D. T. Duong, V. Ho, Z. Shang, S. Mollinger, S. C. B. Mannsfeld, J. Dacuña, M. F. Toney, R. Segalman and A. Salleo, *Adv. Funct. Mater.*, 2014, **24**, 4515–4521.

43 J. Jia, Q. Huang, T. Jia, K. Zhang, J. Zhang, J. Miao, F. Huang and C. Yang, *Adv. Energy Mater.*, 2022, **12**, 2103193.

44 I. Jalan, C. F. N. Marchiori, Z. Genene, A. Johansson, C. Moyses Araujo, E. Wang, J. van Stam and E. Moons, *J. Mater. Chem. C*, 2023, **11**, 9316–9326.

45 Y. Liu, A. Yangui, R. Zhang, A. Kiligaridis, E. Moons, F. Gao, O. Inganäs, I. G. Scheblykin and F. Zhang, *Small Methods*, 2021, **5**, 2100585.

46 N. Yao, Q. Fan, Z. Genene, H. Liu, Y. Xia, G. Wen, Y. Yuan, E. Moons, J. van Stam, W. Zhang, X. Lu, E. Wang and F. Zhang, *Sol. RRL*, 2023, **7**, 2201134.

47 Y. Liu, Q. Fan, H. Liu, I. Jalan, Y. Jin, J. van Stam, E. Moons, E. Wang, X. Lu, O. Inganäs and F. Zhang, *J. Phys. Chem. Lett.*, 2022, **13**, 11696–11702.

48 Q. Fan, R. Ma, T. Liu, J. Yu, Y. Xiao, W. Su, G. Cai, Y. Li, W. Peng, T. Guo, Z. Luo, H. Sun, L. Hou, W. Zhu, X. Lu, F. Gao, E. Moons, D. Yu, H. Yan and E. Wang, *Sci. China: Chem.*, 2021, **64**, 1380–1388.

49 Z. Genene, J.-W. Lee, S.-W. Lee, Q. Chen, Z. Tan, B. A. Abdulahi, D. Yu, T.-S. Kim, B. J. Kim and E. Wang, *Adv. Mater.*, 2022, **34**, 2107361.

50 B. Johs and J. S. Hale, *Phys. Status Solidi A*, 2008, **205**, 715–719.

51 Z. Hamid, A. Wadsworth, E. Rezasoltani, S. Holliday, M. Azzouzi, M. Neophytou, A. A. Y. Guilbert, Y. Dong, M. S. Little, S. Mukherjee, A. A. Herzing, H. Bristow, R. J. Kline, D. M. DeLongchamp, A. A. Bakulin, J. R. Durrant, J. Nelson and I. McCulloch, *Adv. Energy Mater.*, 2020, **10**, 1903248.

52 W. Zhang, Y. Yue, R. Yang, Y. Zhang, W. Du, G. Lu, J. Zhang, H. Zhou, X. Zhang and Y. Zhang, *Energy Environ. Sci.*, 2024, **17**, 2182–2192.

53 Y. Wang, X. Wang, B. Lin, Z. Bi, X. Zhou, H. B. Naveed, K. Zhou, H. Yan, Z. Tang and W. Ma, *Adv. Energy Mater.*, 2020, **10**, 2000826.

54 C. Chen, G. Wen, Z. Xiao, J. Peng, R. Hu, Z. Chen, C. Zhang and W. Zhang, *Photonics*, 2022, **9**, 892.

55 G. Wen, R. Hu, J. Feng, J. Peng, Z. Chen, C. Zhang, N. Zhao, X. Zou, Z. Chen, C. Liu and W. Zhang, *Chem. Eng. J.*, 2023, **475**, 145939.

56 Z. Chen and H. Zhu, *J. Phys. Chem. Lett.*, 2022, **13**, 1123–1130.

57 J. Feng, G. Wen, R. Hu, J. Peng, H. Lu, N. Zhao, X. Zou and W. Zhang, *Sol. RRL*, 2023, **7**, 2300372.

58 Z. Xu, K. S. Park, J. J. Kwok, O. Lin, B. B. Patel, P. Kafle, D. W. Davies, Q. Chen and Y. Diao, *Adv. Mater.*, 2022, **34**, 2203055.

This journal is © The Royal Society of Chemistry 2024

J. Mater. Chem. C, 2024, **12**, 13029–13039 | **13039**